Research Square

Preprints are preliminary reports that have not undergone peer review.
They should not be considered conclusive, used to inform clinical practice,
or referenced by the media as validated information.

Label-free morphometric profiling reveals early drug responses in 3D tumor spheroids

Rosario Fernandez-Godino

rosario.fernandez@medinaandalucia.es

Fundación Medina

Inmaculada Iañez García

Fundación Medina

Marta Martínez García

Fundación Medina

Maria C Ramos

Fundación Medina

Article

Keywords: high-content imaging, machine learning, 3D models, triple negative breast cancer, phenotypic profiling

Posted Date: May 13th, 2026

DOI: https://doi.org/10.21203/rs.3.rs-9208673/v1

License: This work is licensed under a Creative Commons Attribution 4.0 International License.
Read Full License

Additional Declarations: No competing interests reported.

Version of Record: A version of this preprint was published at Scientific Reports on October 5th, 2026. See the published version at https://doi.org/10.1038/s41598-026-74860-2.

Abstract

Quantitative and scalable analysis of drug responses in three-dimensional (3D) tumor models remains a major challenge for phenotypic drug discovery. Here, we present *m3DinAI Drug Quest*, a label-free high-content imaging (HCI) framework for longitudinal morphometric profiling of tumor spheroids. Using brightfield imaging combined with multiparametric feature extraction, we generate time-resolved phenotypic signatures of triple-negative breast cancer (TNBC) spheroids treated with chemotherapeutic agents spanning distinct mechanisms of action.

To quantify early drug-induced effects, we introduce the **morphological disruption concentration (MDC)**, defined as the minimal dose that induces reproducible structural alterations in 3D spheroids. MDC reveals drug responses not captured by conventional viability assays and consistently indicates increased drug tolerance in 3D compared with 2D cultures. Unsupervised dimensionality reduction using Uniform Manifold Approximation and Projection (UMAP) further identifies treatment-specific morphological signatures that distinguish drug classes based on label-free imaging data.

Together, these results establish label-free morphometric profiling as a scalable approach for characterizing drug responses in 3D tumor models and position MDC as a complementary metric to conventional potency measurements. This framework is readily applicable to diverse 3D culture systems, including patient-derived models.

1. Introduction

Three-dimensional (3D) tumor models, including spheroids, recapitulate key features of solid tumors like cellular heterogeneity, cell-cell interactions, and diffusion gradients more accurately than conventional two-dimensional (2D) cultures[1,2]. Unfortunately, quantitative analysis of drug responses in 3D spheroids remains methodologically challenging. Classical assays rely on endpoint viability measurements or fluorescence-based readouts, which provide bulk signals and often fail to capture early or structural phenotypic changes. To address this limitation, we present *m3DinAI Drug Quest*, a label-free high content imaging (HCI) framework for longitudinal monitoring of spheroids using brightfield microscopy. Unlike single-parameter viability readouts, computational HCI analyses generate rich multiparametric datasets that capture spheroid morphology, growth dynamics, and structural integrity through a wide range of morphological features. These datasets provide insights not only into cell viability but also into drug-induced phenotypic changes specific to 3D systems, such as compaction, disintegration, or necrotic core formation [3]. To quantify these changes, we introduce the morphological disruption concentration (MDC), defined as the minimal drug dose required to induce reproducible structural alterations in 3D tumor spheroids. MDC is conceptually analogous to the half-maximal effective concentration (EC_{50}) used in 2D assays, but it is designed to capture early phenotypic responses that precede overt loss of viability and reflect subtle changes in spheroid architecture.

To interpret high-dimensional feature data, we apply unsupervised dimensionality reduction using Uniform Manifold Approximation and Projection (UMAP), enabling visualization of treatment-associated phenotypic states and comparison across conditions. This approach allows the identification of drug-specific morphological signatures and facilitates classification of phenotypic responses according to mechanism of action (MoA) [4].

To validate *m3DinAI* in a biologically relevant 3D cancer setting, we used triple negative breast cancer (TNBC) spheroids derived from three established cell lines representing distinct molecular and phenotypic subtypes. Spheroids were treated with a panel of chemotherapeutic agents spanning four major mechanistic classes -antimetabolites, anthracyclines, topoisomerase inhibitors, and taxanes- representing standard breast cancer therapies. Phenotypic profiles were generated using brightfield HCI followed by automated image processing, feature extraction, and unsupervised analysis [3]. Extracted descriptors included shape, texture, and radiomic features[3,5] enabling quantitative comparison of treatment-induced phenotypic states across time points and cell lines [5–7].

By combining label-free HCI, multiparametric feature extraction, and unsupervised embedding, *m3DinAI Drug Quest* provides a scalable framework for quantifying drug-induced phenotypic responses in 3D tumor models.

2. Results

2.1. Drug-induced toxicity in TNBC 2D cultures

As a conventional benchmark for comparison with 3D phenotypic profiling, dose–response experiments were performed in 2D cell cultures of the TNBC cell lines BT-549, HCC1806, and MDA-MB-468 treated for 72 h with the selected chemotherapeutic agents: antimetabolites [gemcitabine (GEM), 5-fluorouracil (5-FU)], anthracyclines [doxorubicin (DOX), epirubicin (EPI)], topoisomerase inhibitors [etoposide (VP-16), camptothecin (CPT)], and taxanes [docetaxel (DTX), and paclitaxel (PTX)]. EC_{50} values of each drug were determined at 72 h by MTT (3-(4,5-dimethylthiazol-2-yl)-2,5-diphenyl tetrazolium bromide) viability assay **(**Table 1**)**. All samples were analyzed in triplicate. Colorimetry data was analyzed by Genedata Screener, showing Z'-factor values higher than 0.6, and signal-to-background ratios higher than 6 for the three cell lines **(Supplementary Fig. 1).**

Table 1

EC_{50} values with 95% confidence intervals (IC95%) for chemotherapeutic agents in 2D cultures of the three TNBC cell lines. EC_{50} [μM] ± IC95% derived from 12-point, 1:2 serial dilution curves in BT-549, HCC1806, and MDA-MB-468 cells after 72 h treatment. Compounds not reaching full inhibition within the maximum concentration allowed by DMSO solubility (0.5% v/v) are reported as higher than (>) their highest tested dose.

Drug Class	EC_{50} ± IC95%[μM]			
	Compound	BT-549	HCC1806	MDA-MB-468
Antimetabolite	GEM	3.70 ± 3.63	0.109 ± 0.019	0.46 ± 0.09
Antimetabolite	5-FU	> 200.00	> 200.00	103.51 ± 20.63
Anthracycline	DOX	7.11 ± 4.35	14.04 ± 7.35	3.63 ± 0.58
Anthracycline	EPI	2.12 ± 2.39	6.54 ± 2.77	2.79 ± 0.79
Topoisomerase Inh	VP-16	8.51 ± 2.24	20.18 ± 6.69	37.92 ± 13.54
Topoisomerase Inh	CPT	1.22 ± 0.28	0.63 ± 0.12	1.44 ± 0.65
Taxane	DTX	0.022 ± 0.004	0.0064 ± 0.0006	0.0096 ± 0.0030
Taxane	PTX	0.65 ± 0.11	0.38 ± 0.13	0.58 ± 0.23

In general, comparable activity profiles were obtained across the three cell lines for each drug class. Taxanes showed the highest antitumoral efficacy for the three TNBC cell lines, reaching the low nanomolar or even sub-nanomolar range for DTX and mid-nanomolar for PTX (Table 1). Anthracyclines and topoisomerase inhibitors showed weak activity in the low micromolar range. Notably, CPT showed 7- to 36-fold greater potency than etoposide (VP-16), highlighting substantial differences in the effect of drugs with similar MoA. A similar divergence was observed among antimetabolites, with GEM showing moderate to low potency whereas 5-FU was inactive under the conditions tested. Overall, the observed hierarchy of drug sensitivity was taxanes > camptothecin > anthracyclines/etoposide > gemcitabine > 5-FU.

2.2. Label-free morphometric profiling of 3D spheroids using *m3DinAI*

2.2.1. Characterization of drug-induced toxicity in TNBC 3D spheroids

For 3D cell cultures, assessing cell viability via EC_{50} at a single endpoint would imply an oversimplification of the drug-induced effects. HCI allows for a better quantification of drug toxicity in 3D cultures by combining image acquisition, segmentation, and multiparametric feature extraction, which determines not only viability but also structural damage over time. With this in mind, we first characterized the morphological changes of reference spheroids treated with MMS and DMSO. A total of 32 replicate wells per plate were used for each control. As expected, MMS induced loss of

morphological integrity across the three TNBC spheroids, with varing degrees of fragmentation or collapse, while DMSO-treated spheroids maintained their compactness and uniform structure over 72 hours of treatment **(Supplementary Fig. 2)**. These control states provided a robust phenotypic baseline for comparative treatment analyses.

Interestingly, each cell line displayed a unique baseline 3D architecture and treatment response pattern. For instance, BT-549 cells formed compact and homogeneous spheroids, with minimal yet measurable changes observed after MMS treatment; whereas HCC1806 spheroids were moderately cohesive and less compact, and presented a distinct reflective outer ring that was disrupted by MMS, resulting in enlarged spheroids. In contrast, MDA-MB-468 cells aggregated forming loose and variable spheroids that spread after MMS treatment, building a characteristic 3D phenotype **(**Fig. 1**).** Such variability was a fair representation of the biological diversity observed in TNBC tumors, and supported the use of HCI in advanced cell models with diverse architectures.

To quantify the drug-induced changes observed in tumor spheroids, *m3DinAI Drug Quest* relies on a Python-based image analysis pipeline that extracts morphometric and textural features from HCI brightfield images to define spheroid phenotypic profiles, structural integrity, and drug-induced disruption. For each of the eight chemotherapeutic agents, dose-response experiments were performed in BT-549, HCC1806 and MDA-MB-468 spheroids, using the same 12 concentrations tested in 2D cultures with three replicates per dose. Plates were imaged 72 hours after treatment.

We next evaluated the ability of *m3DinAI* to characterize morphological variations, ranging from intact, compact spheroids to highly disrupted structures. The segmentation workflow was qualitatively assessed using contour overlays on representative images from each cell line treated with DMSO and MMS. Across the three TNBC models, contour overlays showed accurate boundary detection and consistent delineation of spheroid areas, despite differences in cohesion and structural integrity **(Supplementary Fig. 2).** These results confirmed the ability of the algorithm to successfully track morphological alterations induced by cytotoxic stress (MMS control) while avoiding systematic under- or over-segmentation artefacts.

Morphometric, texture, and radiomic features were extracted from all segmented spheroids to generate a multiparametric phenotypic representation of each model. These descriptors included classical geometric m easurements,texture statistics, and high-dimensional radiomic features derived from PyRadiomics (see the materials and methods section) [5,8–10]. The consistency and discriminative capacity of the selected shape features was determined using descriptive violin plots **(**Fig. 2**)**. This illustrative visualization allowed comparing feature distributions across cell lines and identifying differences in spheroid morphology. Violin plots revealed a narrow, sharply peaked distribution of projected area and perimeter for BT-549 spheroids consistent with their compact and uniform growth, compared to MDA-MB-468 spheroids, which displayed broader, right-skewed distributions, reflecting their loose, heterogeneous aggregation patterns **(**Fig. 2**)**. The consistent sphericity of BT-549 was demonstrated by the distribution of circularity (0.5-1), compared to HCC1806 (0.2–0.5) and MDA-MB-

468 (< 0.3), which showed an irregular shape. Similarly, solidity distinguished BT-549 as the most condensed spheroids (values concentrated near 1), followed by HCC1806 with intermediate values, and MDA-MB-468 with lower solidity reflecting more concave and irregular structures. Extent (overall spatial spread of the spheroid in the image field) showed high, concentrated values close to 1 for BT-549, indicating minimal empty space, compared to HCC1806 (0.6–0.9), or MDA-MB-468 (0.2-1), consistent with their loose edges and poorly cohesive aggregates. The aspect ratio distribution showed that BT-549 and HCC1806 spheroids largely maintained isotropic shapes with values close to 1, while MDA-MB-468 exhibited a wider range of aspect ratios, reflecting occasional elongation or shape distortion. Finally, the major and minor axis lengths corroborated these observations, confering BT-549 spheroids consistent dimensions compared to HCC1806, which showed modest changes and MDA-MB-468, which larger values indicate more disperse and irregular structures. Altogether, these results indicate that the feature set extracted by *m3DinAI* captures biologically meaningful architectural differences across 3D spheroid models.

2.2.2. Technical reproducibility of HCI analyses by m3DinAI Drug Quest

To assess the technical reproducibility of the assay, inter-plate biological replicates were performed over different weeks. The distributions of key morphological features, including area, perimeter, circularity, solidity, extent, aspect ratio, major axis, and minor axis, were measured across 48 replicate spheroids at 72 h post-treatment. Highly similar patterns were observed across replicates for most features, supporting the robust segmentation and consistent feature extraction regardless of the cell line or drug treatment **(**Fig. 3**)**. These results support the strong reproducibility of *m3DinAI* to precisely characterize spheroid morphology using brightfield HCI data.

2.2.3. Morphological Disruption Concentration (MDC)

Given the complexity of 3D spheroid architecture, and with the aim of capturing even minimal drug-induced change, we introduce the concept of MDC, defined as the lowest drug concentration that consistently induces subtle but measurable changes in the 3D phenotype. Importantly, these changes may precede overt structural collapse at higher doses, making MDC a sensitive readout for early treatment-associated perturbations in complex 3D architectures.

Before quantifying the effect of each drug in the spheroids, we verified that the extracted features reflected treatment-dependent differences. To this end, a dimensionality reduction approach was applied using UMAP and k-means clustering (k = 2 clusters), projecting the high-dimensional feature space into a two-dimensional space. This representation allowed to classify spheroids into affected and non-affected phenotypic states, as represented on the plate-based heatmap (Fig. 4**)**. Binary labels for “disrupted” (red) *versus* “intact” (blue) phenotypes were assigned by anchoring the two clusters to the MMS-treated and DMSO-treated controls, respectively. Using this framework, the MDC was determined as the first dose at

which all biological replicates were classified into the “disrupted/red” cluster (Fig. 4). The resulting MDC values for each drug and cell line are shown in Table 2.

Table 2
MDC for chemotherapeutic agents in 3D spheroid models. Summary of MDC values [μM] estimated for eight chemotherapeutic agents tested across BT-549, HCC1806, and MDA-MB-468 spheroids.

Drug Class	MDC [μM]			
	Compound	BT-549	HCC1806	MDA-MB-468
Antimetabolite	GEM	100	3.1	100
Antimetabolite	5FU	> 200	> 200	> 200
Anthracycline	DOX	62.5	0.5	3.9
Anthracycline	EPI	27.5	0.4	3.4
Topoisomerase Inh	VP-16	50	25	50
Topoisomerase Inh	CPT	5	2.5	0.6
Taxane	DTX	0.0005	0.0005	> 1
Taxane	PTX	0.005	0.005	> 10

To compare drug responses in 3D and 2D settings, the MDC values were examined alongside the EC_{50} reported in the Table 1. Across treatments and cell lines, MDC values were generally shifted toward higher concentrations compared to the EC_{50} values, reflecting the greater treatment tolerance observed in 3D spheroids (Fig. 5). Importantly, MDC and EC_{50} are not equivalent measurements: MDC captures the earliest reproducible morphological perturbation in 3D spheroids, whereas EC_{50} reflects loss of viability in 2D monolayer cultures. Even so, the systematic increase in MDC relative to EC_{50} illustrates how 3D architecture modulates drug response in ways that are not captured by conventional monolayer assays [11–13]. The extent of this shift varied across cell lines and treatments, supporting the view that spheroid architecture influences the magnitude and nature of drug-induced phenotypic change. Notably, taxanes retained comparatively strong activity in the more compact BT-549 and HCC1806 spheroids, indicating that the impact of 3D organization on drug response is treatment-dependent rather than uniform across pharmacological classes. This particular result may be a consequence of the presence of a differentiated outer rim of proliferating cells in these spheroids, where taxanes exert stronger cytotoxic effects by stabilizing microtubules and interfering with cell division [14,15]. BT-549 spheroids, with their dense, homogeneous structure, present the greatest barrier to diffusion, restricting access of antimetabolites and DNA-damaging agents to the actively cycling rim and conferring broad resistance. HCC1806 spheroids, less compact and more permeable, allow deeper drug penetration and sustain higher fractions of proliferating cells, accounting for their overall sensitivity. While MDA-MB-468

spheroids, with loose and irregular cell aggregates, represent an intermediate state, where partial penetration and heterogeneous cell cycling produce moderate resistance.

2.3. Time-resolved profiling of the phenotypic responses to chemotherapy in TNBC spheroids

The decreased effect of most drugs in 3D compared to 2D cultures raised the hypothesis of a reduced penetration and diffusion of drugs through cell layers. To further characterize treatment-induced phenotypic changes over time, exposure was extended to 96 and 120 h for compounds with nanomolar to low micromolar MDC values (Fig. 6), which exluded the antimetabolites (Table 2). Drug effects were quantified using an *Activity Ratio* (AR) metric that measured the position of each well relative to control phenotypes. DMSO-treated spheroids remained morphologically stable over time in all cell lines, establishing a reliable baseline for longitudinal analysis. Briefly, all features were z-score standardized, and the DMSO and MMS centroids were calculated as the mean feature vectors of their respective control wells. The AR for each well was then obtained using the Euclidean distance (d) to each centroid according to the formula (1):

$$\text{Activity Ratio} = \left(\frac{\text{dDMSO}}{\text{dDMSO} + \text{dMMS}} \right) \times 100$$

1

Higher AR values indicate lower similarity to the DMSO-associated phenotype and closer to the MMS-induced phenotype. Compared with untreated controls, spheroids treated with all chemotherapeutic agents displayed structural alterations whose magnitude and timing depended on both drug class and cell line. BT-549 spheroids, initially compact and showing higher MDC values (Table 2), displayed detectable phenotypic effects from 72 h of treatment that remained stable over time (Fig. 6). HCC1806 spheroids exhibited subtler but persistent structural changes over time, consistent with their higher overall susceptibility (lowest MDC, Table 2). MDA-MB-468 spheroids showed more modest morphological changes, reflecting their loose baseline architecture, with profiles more similar to DMSO controls, which became more significant at 120 h. In this model, anthracyclines produced more evident effects whereas taxanes showed limited activity.

AR integrates the full feature set into a single quantitative score, providing a precise and reproducible measure of phenotypic displacement across independent assays, with low standard deviation, indicating high reproducibility among different assays and plates. Together, these results demonstrate the ability of *m3DinAI* to capture the temporal evolution of treatment responses and to resolve drug class- and architecture-dependent dynamics in 3D spheroids.

2.4. UMAP resolves treatment-specific morphological signatures in 3D TNBC spheroids

To determine whether *m3DinAI* could define treatment-associated phenotypic profiles from high-dimensional imaging data, we applied UMAP, an unsupervised dimensionality reduction method, to embed spheroid features into a low-dimensional space while preserving both local and global feature relationships among samples. This analysis generated phenotypic maps in which spheroids grouped according to shared morphological states, revealing clusters associated with specific drug responses **(**Fig. 7**)**. To assess the reproducibility and consistency of these signatures across cell lines and time points, a pooled UMAP embedding was generated by jointly analyzing feature data from all intra- and inter-plate replicates. In this representation, treatments were coded by color and biological replicates were distinguished by marker symbols **(**Fig. 7**).**

Treatment groups, including controls, formed well-defined and consistently separated clusters, indicating that each drug induced a characteristic and reproducible morphological signature **(**Fig. 7**)**. Replicate markers were distributed within each treatment -associated clusters rather than forming separate groups or outliers, supporting the absence of evident replicate-specific batch effects. In BT-549 spheroids, the architectural changes quantified by AR from 72 h onward **(**Fig. 6**)** were reflected in distinct clusters associated with each treatment **(**Fig. 7a**)**. In this model, separation by MoA was already evident at 72 h **(Supplementary Fig. 3)**. Notably, anthracyclines separated into two subclusters corresponding to DOX and EPI, suggesting that *m3DinAI* can resolve phenotypic differences even within the same pharmacological class. For HCC1806 spheroids, taxanes formed discrete clusters, whereas anthracyclines and topoisomerase inhibitors partially overlapped, consistent with their interrelated MoA.[16–19] Of note, taxanes clustered between topoisomerase inhibitors and DMSO, confirming the intermediate activity observed in the AR **(**Fig. 6**)**. In MDA-MB-468 spheroids, taxanes clustered together with DMSO-treated controls, validating the data observed in the AR, which showed no significant activity for this drug class in this cell line. Topoisomerase inhibitors showed a subtle effect, as measured by the AR **(**Fig. 6**)**, which explains their clustering close to the DMSO-treated controls; while anthracyclines showed a distinct effect and grouped separately, as expected based on their significantly elevated AR **(**Fig. 6**)**. The disrupted architecture of the MDA-MB-468 spheroids occasionally hampered the segmentation process, which explains the appearance of a small outlier group in the anthracyclines treatment **(**Fig. 7c**)**.

Unlike fluorescence-based pipelines, *m3DinAI* levarages these treatment-specific and cell line-specific phenotypic signatures, combined with the MDC and AR to monitor the temporal progression of drug-induced perturbations in living spheroids **(Supplementary Fig. 3)**.

3. Discussion

Our study establishes *m3DinAI Drug Quest* as a robust and reproducible label-free platform for high-content phenotypic profiling of drug responses in 3D tumor spheroids. By combining brightfield imaging with automated extraction of geometric, textural, and radiomic features, *m3DinAI* captures minimal structural perturbations that are not resolved by conventional metabolic-based viability assays. [2,3,5] This

framework enables the generation of interpretable phenotypic signatures associated with treatment response, supporting discrimination of drug classes by MoA.

The results of this study reflect the intrinsic protection of three-dimensional human tumors against chemotherapy, supporting the relevance of 3D versus 2D cell cultures for cancer drug discovery. To account for tumor variability, we chose three TNBC cell lines that differ in origin, molecular subtype, and morphology. For instance, BT-549 contains structures that support cell-cell adhesion, which may explain its compactness and the higher MDC needed to disrupt these spheroids. [20,21] Contrarily, MDA-MB-468 has a high capacity of DNA repair [22], which confers an increased tolerance to taxanes and topoisomerase inhibitors, consistent with the high MDC values observed, while HCC1806 is more vulnerable to both cytotoxic and cytoskeletal-disrupting agents. [23–25]

It is important to highlight that *m3DinAI* can resolve meaningful differences within pharmacological classes that are not reflected by conventional cytotoxicity assays. This is supported by the differences observed in MDC between the two taxanes and the two topoisomerase inhibitors, reflecting their different pharmacology,[16] while anthracyclines with similar chemistry displayed comparable MDC values. [26] However, the two anthracyclines clustered apart in the UMAP projections (Fig. 7a), likely reflecting their distinct intracellular pharmacology mediated by specific transporters. [26]

Through its label-free design, *m3DinAI* possibilites monitoring dynamic phenotypic changes, missed by single end-point metabolic assays that can misrepresent drug efficacy due to metabolic adaptation. [27–29] Instead, *m3DinAI* uses MDC to determine the lowest concentration needed to cause a morphological change, and AR to rank the intensity and durability of each perturbation over time. Subsequent implementation of UMAP projections allows the identification of specific drug-induced signatures, proving that the morphological changes captured by MDC and AR are not arbitrary but coherent with the MoA. [5–9] Together, these features give *m3DinAI* clear translational potential for phenotypic drug profiling in cancer spheroids, particularly in settings such as TNBC where actionable molecular targets are limited. In the context of patient-derived organoids (PDOs), the platform could be extended to support rapid functional profiling and compound prioritization based on baseline architecture and treatment-induced phenotypic response. [11–13,30,31]

Beyond single-agent testing, *m3DinAI* could be adapted to drug combination studies and sequential treatment regimens, where temporal phenotypic profiling may reveal synergistic or antagonistic interactions not detected by conventional assays. In addition, the ability to derive treatment-associated phenotypic clusters without molecular labeling supports its application in high-throughput screening of novel or repositioned compounds with diverse or incompletely characterized MoA.

4. Conclusion

This study establishes *m3DinAI* as a label-free phenotypic profiling platform for characterizing chemotherapeutic responses in 3D tumor spheroids. Our results show that HCI morphometric features

capture distinct and reproducible treatment-associated phenotypic signatures across cell lines and drug classes that are not captured by classical cell viability assays. By combining MDC, AR, and unsupervised embedding, *m3DinAI* detects early structural perturbations and organizes compounds with similar MoA according to shared phenotypic response patterns over time. This framework is applicable to a wide range of 3D culture systems, including patient-derived models.

5. Materials and Methods

5.1. Cell lines and reagents

Human TNBC cell lines BT-549 (HTB-122), HCC1806 (CRL-2335) and MDA-MB-468 (HTB-132) were purchased from ATCC (American Type Culture Collection, Manassas, VA, USA). BT-549 and HCC1806 were maintained in RPMI-1640 medium (Biowest™. Nuaille, France) supplemented with 10% fetal bovine serum (FBS) (Gibco™), 1% penicillin–streptomycin (Gibco™), and 0.023 U/mL recombinant human insulin (Sigma-Aldrich™. St. Louis, MO, USA), for BT-549. MDA-MB-468 was maintained in Leibovitz's L-15 medium with 10% FBS. All cells were cultured in a humidified 37°C incubator with 5% CO_2.

5.2. Cell cultures and drug treatments

Eight chemotherapeutic agents: gemcitabine (GEM; cat. G6423), 5-fluorouracil (5-FU; cat. F6627), etoposide (VP-16; cat. 341205), camptothecin (CPT; cat. C9911), doxorubicin (DOX; cat. D1515), epirubicin (EPI; cat. E9406) and paclitaxel (PTX; cat. T7191), all purchased from Sigma-Aldrich™ (Merck), and docetaxel (DTX; cat. 4056, Tocris™ [Bio-Techne, Bristol, United Kingdom]), belonging to four drug classes commonly used in in the clinic[32,33]: antimetabolites[34], cytotoxic antibiotics (anthracyclines)[35], topoisomerase inhibitors[36], and microtubule-targeting agents (taxanes)[37] were resuspended in 100% DMSO and concentrations were adjusted following previously published in vitro studies[38,39]: GEM 100 µM, 5-FU 200 µM, DOX 250 µM, EPI 110 µM, VP-16 50 µM, CPT 10 µM, DTX 1 µM, PTX 10 µM. Drugs were added to the cell culture plates at a final DMSO concentration of 0.5% (v/v). MMS (methyl methanesulfonate), resuspended in DMSO, and DMSO were used as positive and negative controls, respectively.

5.2.1. Cell viability assays (2D cultures)

For 2D assays, BT-549, HCC1806, and MDA-MB-468 were seeded in 384-well µClear® plates (Greiner, Kremsmünster, Austria, cat. 781096) at a density of 2,000–3,000 cells/well using a Multidrop™ Combi (Thermo Scientific, Waltham, Massachusetts, US) in 20 µL. Dose–response experiments were conducted for each cell line, using 12 doses in triplicate, with 1:2 dilutions. DMSO 0.5% was used as control vehicle and 4 mM MMS as a positive cytotoxic control. The EC_{50} was determined after 72 hours of treatment using MTT viability assay (3-(4,5-dimethylthiazol-2-yl)-2,5-diphenyl tetrazolium bromide, ACROS Organics, Thermo Scientific), a well-established colorimetric method that measures mitochondrial metabolic activity via reduction of MTT to insoluble formazan crystals[40]. Following 4 h of incubation at 37°C,

absorbance was recorded at 570 nm using an EnVision Multilabel Plate Reader (Revvity, Waltham, Massachusetts, US). EC_{50} values were calculated by nonlinear regression with Genedata Screener (v21.0.1-Standard) using a Smart Fit model selection (Constant or Hill).

5.2.2. High-Content Imaging (HCI) (3D cultures)

For 3D spheroids, BT-549, HCC1806, and MDA-MB-468 cells were seeded in 384-well ultra-low attachment (ULA) Corning® 384-well spheroid microplates (cat. 4516, black-walled, round-bottom, hydrogel-coated) at a density of 2,500-5,000 cells/well using a Multidrop™ Combi (Thermo Scientific). Plates were centrifuged at 400 × g for 5 min and incubated at 37°C, 5% CO_2, for 24 h to ensure spheroid formation. Dose-response curves were conducted using the same concentrations and controls as described for 2D assays, employing a 1:2 serial dilution series performed in triplicate at each drug concentration (three technical replicates per dose). For the clustering dataset, experiments included three independent replicate plates, corresponding to 48 replicate spheroids per drug–dose condition. Image acquisition was performed using the Operetta CLS™ High-Content Analysis system (Revvity) with the 10× objective in confocal mode. Spheroids were imaged exclusively in brightfield (BF) mode, as no fluorescence labeling was applied. High-Content Images (HCI) were acquired at 72 h, 96 h, and 120 h after treatment at a resolution of 1080 × 1080 pixels, with a spatial resolution of 3938 dpi and 16-bit depth, using a PerkinElmer 1600L20344 camera. Each plane was saved in TIFF format (LZW-compressed, grayscale, single-channel). Plates were fully scanned and all acquisition parameters—objective, number of planes, Z-step size, and illumination settings—were kept constant across experimental conditions to ensure data consistency. Raw image stacks were organized and transferred to a dedicated working directory. Pre-processing steps followed a reproducible pipeline: **1) Maximum intensity projection (MIP)**: For each well, a Z-stack of 15 optical planes was acquired with a step size of 7.5 µm, allowing full volumetric capture of the spheroid structure. Each Z-stack was collapsed into a 2D projection image[41]; **2) Bit-depth conversion and contrast normalization**: Projected images (16-bit TIFF format) were converted to 8-bit to enhance contrast for segmentation; **3) Segmentation and mask generation**: Normalized 8-bit images were filtered with a Gaussian blur to reduce background noise, followed by thresholding using Otsu's method. Morphological opening with a 3×3 kernel removed small artifacts, and external contours corresponding to spheroid boundaries were identified. Binary masks were generated and saved in parallel with the projected images for subsequent feature extraction. Overlaid contour images were also exported to facilitate quality control.

As a quality control step for segmentation and feature extraction, binary masks were generated and overlays of the contours on the original BF images were generated for each spheroid. Random overlays were visually inspected to confirm accurate boundary detection and segmentation consistency. No images were excluded at this stage.

5.3. HCI data analyses

5.3.1. Feature extraction

A total of 144 features were extracted from high content images as follows:

a. 8 shape features: Area (px²) (calculated from the total pixel count within the contour, converted to real-world area using pixel calibration from the imaging system), perimeter (px) (calculated as the arc length of the detected contour), circularity (4π × (Area) / (Perimeter²)), solidity (ratio of the spheroid area to its convex hull area, indicating concavity and surface irregularities), extent (proportion of the bounding box area occupied by the spheroid area), aspect ratio (major axis divided by minor axis from an ellipse fitted to the contour, measuring elongation), bounding box dimensions (width, height), Hu moments Hu1–Hu7 (set of seven scale- and rotation-invariant shape descriptors derived from the central moments of the contour). As an internal consistency check, the measured projected areas in pixel²/px^2 were cross-validated against spheroid diameters obtained from raw images using the Harmony software (Revvity). The approximate relationship between measured diameters and contour-based areas was verified using the standard circular area formula, confirming agreement within the expected range of natural spheroid shape irregularities.

b. 27 Texture features: Quantitative texture analysis was conducted on grayscale images of the spheroids using the *scikit-image* (v0.20.0) and *Mahotas* (v1.4.13) Python libraries. Prior to feature extraction, all images were preprocessed with a mild Gaussian blur to mitigate salt-and-pepper noise while preserving textural details. Texture features were derived using three complementary approaches: 1) Four Gray Level Co-occurrence Matrix (GLCM) features (contrast, correlation, energy, and homogeneity) were computed using a pixel pair distance of 1 and an orientation of 0°, based on a symmetric and normalized co-occurrence matrix, 2) Ten Local Binary Pattern (LBP) descriptors were extracted using the uniform pattern method with a radius of 1 and 8 sampling points and summarized into 10 histogram bins, encompassing both uniform and non-uniform (noise) patterns, **3)** Thirteen classical Haralick texture descriptors, including entropy, variance, and others, were computed.
c. 102 Radiomics features: To extend the feature space, *PyRadiomics* (v3.0.1) library was employed, using the same grayscale images and the binary masks generated from segmentation. All feature classes available in *PyRadiomics* were enabled (9 shape 2D, 18 first-order statistics, 24 GLCM, 16 GLSZM features, 16 GLRLM, 14 GLDM, and 5 NGTDM), ensuring a high-dimensional and interpretable radiomic profile. Prior to extraction, images and masks were converted from *NumPy* arrays to *SimpleITK* images to comply with *PyRadiomics* requirements. The resulting dictionary of features was parsed and appended to the master feature table.

The complete feature set was assembled in a *pandas* DataFrame (v1.5.3) and exported to Excel format using *openpyxl* for downstream analysis and reproducibility. Next, the median and standard deviation were calculated for each feature within its treatment group and outliers (median ± 3 SD) were excluded using Python 3.10 (pandas (v1.5.3) and NumPy (v1.24.2). Features were then normalized by z-score standardization using the *StandardScaler* module from *scikit-learn* (v1.2.2), applying the Eq. (2):

$$z = \frac{x - \mu}{\sigma}$$

2

Equation: z-score standardization. μ = mean and σ = standard deviation of the feature across the filtered spheroids.

5.3.2. UMAP projections

UMAP, a non-linear manifold learning technique widely used in ML and artificial intelligence (AI) for dimensionality reduction and data visualization, was used to project HCI-extracted morphological features into an interpretable two-dimensional space[42,43]. UMAP constructs a graph of nearest neighbors in the original high-dimensional feature space and optimizes a low-dimensional embedding that preserves this local neighborhood structure while maintaining a meaningful global organization of the data[42]. In our study, UMAP was applied to single-cell morphological profiles to visualize relationships of similarity between treatments and cell lines, enabling the identification of treatment-driven phenotypic clusters, gradients and outliers, as commonly done in high-content and single-cell profiling workflows[43,44]. Two-dimensional UMAP projections were generated using the Python implementation provided by the *umap-learn* library (v0.5.3) and plotted with *Matplotlib* (v3.7.1) and *Seaborn* (v0.12.2). UMAP was configured with 15 nearest neighbors, a minimum distance of 0.1, the default Euclidean distance metric, and a fixed random seed of 42 to ensure reproducibility. These parameters balanced the preservation of local neighborhood structures with adequate global separation of treatment-driven morphological signatures and are in line with previous applications of UMAP to high-dimensional biological datasets[42,43].

Declarations

6. Acknowledgements

We thank Fundación MEDINA and the Andalusian Government for the Funding (Plan Andaluz de Investigación, Desarrollo e Innovación (PAIDI 2020) as part of the Estrategia de Innovación de Andalucía (RIS3 Andalucía, IEPR-0031).

7. Funding

This work was supported by Fundación MEDINA, Centro de Excelencia en Medicamentos Innovadores en Andalucía, Granada (Spain).The Operetta CLS High Content Analysis System was purchased via grants for scientific and technological infrastructures within the Plan Andaluz de Investigación, Desarrollo e Innovación [PAIDI 2020] as part of the Estrategia de Innovación de Andalucía [RIS3 Andalucía, IEPR-0031].

8. Data availability

Reviewer demo datasets are available on Zenodo:

I. Profiling demo dataset (BT549, 72H, R1; DMSO/MMS/Taxane): https://doi.org/10.5281/zenodo.18847934.

II. MDC demo dataset (BT549; 3D spheroids; dose–response plate; DMSO/MMS + drugs): https://doi.org/10.5281/zenodo.18876611.

9. Code availability

All custom Python scripts are openly available at:

https://github.com/InmaIG/m3DinAI and permanently archived on Zenodo (v1.1.1):

https://doi.org/10.5281/zenodo.18889899 [45]

11. Author Contributions

I.I.G. wrote the manuscript, performed experiments, analyzed data, and developed the *m3DinAI* pipeline; M.M.G. contributed to the implementation and optimization of 3D cultures for HTS and helped with experimental work; M.C.R. planned experiments, guided experimental lab work, and edited the manuscript. R.F.G. designed the project, wrote the manuscript, guided the experimental experiments, and coordinated the work.

12. Competing Interests

The authors declare no competing interests.

References

1. Bittman-Soto, X. S., Thomas, E. S., Ganshert, M. E., Mendez-Santacruz, L. L. & Harrell, J. C. *The Transformative Role of 3D Culture Models in Triple-Negative Breast Cancer Research. Cancers* (Multidisciplinary Digital Publishing Institute (MDPI), 2024). 10.3390/cancers16101859
2. Bahcecioglu, G., Basara, G., Ellis, B. W., Ren, X. & Zorlutuna, P. Breast cancer models: Engineering the tumor microenvironment. *Acta Biomater. Acta Mater. Inc*. 1–21. 10.1016/j.actbio.2020.02.006 (2020). PubMed PMID: 32045679.
3. Borten, M. A., Bajikar, S. S., Sasaki, N., Clevers, H. & Janes, K. A. Automated brightfield morphometry of 3D organoid populations by OrganoSeg. *Sci. Rep.* **8** (1). 10.1038/s41598-017- (2018). 18815-8 PubMed PMID: 29593296.
4. Healy, J. & McInnes, L. Uniform manifold approximation and projection. *Nat. Reviews Methods Primers*. **4** (1), 83. 10.1038/s43586-024-00369-5 (2024).
5. Stellato, M. et al. Radiomic analysis of 3D spheroids using 2D brightfield images. *Biomed. Signal. Process. Control*. **103** 10.1016/j.bspc.2024.107366 (2025).

6. Ringers, C. et al. High-content morphological profiling by Cell Painting in 3D spheroids [Internet]. Available from: http://biorxiv.org/lookup/doi/ (2025). 10.1101/2025.02.05.636642 doi:10.1101/2025.02.05.636642.
7. Zhu, S. et al. Influence of experimental variables on spheroid attributes. *Sci. Rep.* **15** (1). 10.1038/s41598-025-92037-1 (2025). PubMed PMID: 40118968.
8. Grexa, I. et al. SpheroidPicker for automated 3D cell culture manipulation using deep learning. *Sci. Rep.* **11** (1). 10.1038/s41598-021-94217-1 (2021). PubMed PMID: 34285291.
9. Vaidyanathan, K. et al. A machine learning pipeline revealing heterogeneous responses to drug perturbations on vascular smooth muscle cell spheroid morphology and formation. *Sci. Rep.* **11** (1). 10.1038/s41598-021-02683-4 (2021). PubMed PMID: 34857846.
10. van Griethuysen, J. J. M. et al. Computational Radiomics System to Decode the Radiographic Phenotype. *Cancer Res.* **77** (21), e104–e107. 10.1158/0008-5472.CAN-17-0339 (2017).
11. Abuwatfa, W. H., Pitt, W. G. & Husseini, G. A. Scaffold-based 3D cell culture models in cancer research. *J. Biomedical Sci. BioMed. Cent. Ltd.* 10.1186/s12929-024-00994 (2024). -y PubMed PMID: 38221607.
12. Shah, S. & D'Souza, G. G. M. Modeling Tumor Microenvironment Complexity In Vitro: Spheroids as Physiologically Relevant Tumor Models and Strategies for Their Analysis. Cells. Multidisciplinary Digital Publishing Institute (MDPI); doi:10.3390/cells14100732. (2025). PubMed PMID: 40422235.
13. Nayak, P., Bentivoglio, V., Varani, M., Signore, A. & Three-Dimensional *In Vitro Tumor Spheroid Models for Evaluation of Anticancer Therapy*: *Recent Updates. Cancers* (Multidisciplinary Digital Publishing Institute (MDPI), 2023). 10.3390/cancers15194846
14. Alalawy, A. I. Key genes and molecular mechanisms related to Paclitaxel Resistance. *Cancer Cell. Int. BioMed. Cent. Ltd.* 10.1186/s12935-024-03415-0 (2024). PubMed PMID: 39003454.
15. Klibaim, S. et al. Enhancing in Vitro anti-metastatic efficacy and deep penetration into tumor spheroid of docetaxel-loaded liposomes via size optimization for prostate cancer treatment. *OpenNano* **22** 10.1016/j.onano.2024.100231 (2025).
16. Skinner, K. T., Palkar, A. M. & Hong, A. L. *Genetics of ABCB1 in Cancer. Cancers* (Multidisciplinary Digital Publishing Institute (MDPI), 2023). 10.3390/cancers15174236
17. Tesauro, C. et al. Topoisomerase i activity and sensitivity to camptothecin in breast cancer-derived cells: A comparative study. *BMC Cancer*. **19** (1). 10.1186/s12885-019-6371-0 (2019). PubMed PMID: 31783818.
18. Thomas, A., Pommier, Y. & American Association for Cancer Research Inc.. Targeting topoisomerase I in the era of precision medicine. Clinical Cancer Research. ; pp. 6581–6589. 10.1158/1078-0432.CCR-19-1089 (2019). PubMed PMID: 31227499.
19. Marinello, J., Delcuratolo, M. & Capranico, G. Anthracyclines as Topoisomerase II Poisons: From Early Studies to New Perspectives. *Int. J. Mol. Sci.* **19** (11), 3480. 10.3390/ijms19113480 (2018).
20. Grantab, R., Sivananthan, S. & Tannock, I. F. The Penetration of Anticancer Drugs through Tumor Tissue as a Function of Cellular Adhesion and Packing Density of Tumor Cells. *Cancer Res.* **66** (2),

1033–1039. 10.1158/0008-5472.CAN-05-3077 (2006).

21. Tseng, L. M. et al. A comparison of the molecular subtypes of triple-negative breast cancer among non-Asian and Taiwanese women. *Breast Cancer Res. Treat.* **163** (2), 241–254. 10.1007/s10549-017-4195-7 (2017).
22. Bai, X., Ni, J., Beretov, J., Graham, P. & Li, Y. Triple-negative breast cancer therapeutic resistance: Where is the Achilles' heel? *Cancer Lett.* **497**, 100–111. 10.1016/j.canlet.2020.10.016 (2021).
23. Prat, A. et al. Molecular Characterization of Basal-Like and Non-Basal-Like Triple-Negative Breast Cancer. *Oncologist* **18** (2), 123–133. 10.1634/theoncologist.2012-0397 (2013).
24. Marra, A., Trapani, D., Viale, G., Criscitiello, C. & Curigliano, G. Practical classification of triple-negative breast cancer: intratumoral heterogeneity, mechanisms of drug resistance, and novel therapies. *NPJ Breast Cancer*. **6** (1), 54. 10.1038/s41523-020-00197-2 (2020).
25. Espinosa Fernandez, J. R. et al. Identification of triple-negative breast cancer cell lines classified under the same molecular subtype using different molecular characterization techniques: Implications for translational research. *PLoS One*. **15** (4), e0231953. 10.1371/journal.pone.0231953 (2020).
26. Camaggi, C. M. et al. Epirubicin and doxorubicin comparative metabolism and pharmacokinetics. *Cancer Chemother. Pharmacol.* **21** (3). 10.1007/BF00262774 (1988).
27. Khalef, L., Lydia, R., Filicia, K. & Moussa, B. *Cell viability and cytotoxicity assays: Biochemical elements and cellular compartments. Cell Biochemistry and Function* (John Wiley and Sons Ltd, 2024). 10.1002/cbf.4007PubMed PMID: 38593323.
28. Sazonova, E. V., Chesnokov, M. S., Zhivotovsky, B. & Kopeina, G. S. Drug toxicity assessment: cell proliferation versus cell death. *Cell. Death Discov*. **8** (1). 10.1038/s41420-022-01207-x (2022).
29. Ghasemi, M., Turnbull, T., Sebastian, S. & Kempson, I. The mtt assay: Utility, limitations, pitfalls, and interpretation in bulk and single-cell analysis. *Int. J. Mol. Sci.* **22** (23). 10.3390/ijms222312827 (2021). PubMed PMID: 34884632.
30. Ascheid, D. et al. A vascularized breast cancer spheroid platform for the ranked evaluation of tumor microenvironment-targeted drugs by light sheet fluorescence microscopy. *Nat. Commun.* **15** (1). 10.1038/s41467-024-48010-z (2024). PubMed PMID: 38678014.
31. Vitacolonna, M. et al. A spheroid whole mount drug testing pipeline with machine-learning based image analysis identifies cell-type specific differences in drug efficacy on a single-cell level. *BMC Cancer*. **24** (1). 10.1186/s12885-024-13329-9 (2024). PubMed PMID: 39696122.
32. Cappuzzo, F. et al. Muiticentric phase II trial of gemcitabine plus epirubicin plus paclitaxel as first-line chemotherapy in metastatic breast cancer. *Br. J. Cancer*. **90** (1), 31–35. 10.1038/sj.bjc.6601518 (2004). PubMed PMID: 14710202.
33. Masuda, N. et al. A phase II study of metronomic paclitaxel/cyclophosphamide/capecitabine followed by 5-fluorouracil/epirubicin/cyclophosphamide as preoperative chemotherapy for triple-negative or low hormone receptor expressing/HER2- negative primary breast cancer. *Cancer*

Chemother. Pharmacol. **74** (2), 229–238. 10.1007/s00280-014-2492-y (2014). PubMed PMID: 24871032.

34. Heinemann, V. Role of Gemcitabine in the Treatment of Advanced and Metastatic Breast Cancer. *Oncology* **64** (3), 191–206. 10.1159/000069315 (2003).
35. Hurvitz, S. A. et al. A careful reassessment of anthracycline use in curable breast cancer. *npj Breast Cancer Nat. Res.* 10.1038/s41523-021-00342-5 (2021).
36. Nitiss, J. L. Targeting DNA topoisomerase II in cancer chemotherapy. *Nat. Rev. Cancer*. 338–350. 10.1038/nrc (2009). 2607 PubMed PMID: 19377506.
37. Škubník, J., Pavlíčková, V., Ruml, T. & Rimpelová, S. *Current perspectives on taxanes: Focus on their bioactivity, delivery and combination therapy. Plants* p. 1–35 (MDPI AG, 2021). 10.3390/plants10030569
38. Stage, T. B., Bergmann, T. K. & Kroetz, D. L. Clinical Pharmacokinetics of Paclitaxel Monotherapy: An Updated Literature Review. *Clin. Pharmacokinet.* **57** (1), 7–19. 10.1007/s40262-017-0563-z (2018).
39. Heggie, G. D., Sommadossi, J. P., Cross, D. S. & Huster, W. J. Diasio2 RB. Clinical Pharmacokinetics of 5-Fluorouracil and Its Metabolites in Plasma, Urine, and Bile1. CANCER RESEARCH. Report. (1987).
40. Mosmann, T. Rapid Colorimetric Assay for Cellular Growth and Survival: Application to Proliferation and Cytotoxicity Assays. Journal oflmmunologicalMethods. Report. (1983).
41. Wardwell-Swanson, J. et al. A Framework for Optimizing High-Content Imaging of 3D Models for Drug Discovery. *SLAS Discovery*. **25** (7), 709–722 (2020). doi:10.1177/2472555220929291 PubMed PMID: 32484408.
42. Mcinnes, L., Healy, J. & Melville, J. *UMAP: Uniform Manifold Approximation and Projection for Dimension Reduction* (Report, 2020).
43. Becht, E. et al. Dimensionality reduction for visualizing single-cell data using UMAP. *Nat. Biotechnol.* **37** (1), 38–47. 10.1038/nbt.4314 (2019). PubMed PMID: 30531897.
44. Way, G. P. et al. Predicting cell health phenotypes using image-based morphology profiling. *Mol. Biol. Cell.* **32** (9), 995–1005. 10.1091/MBC.E (2021). 20-12-0784 PubMed PMID: 33534641.
45. Iáñez García, I. m3DinAI: Morphometric profiling pipeline for 3D TNBC spheroids [Internet]. Zenodo; (2025). Available from: https://doi.org/10.5281/zenodo.17242729 doi:10.5281/zenodo.17242729.

Figures

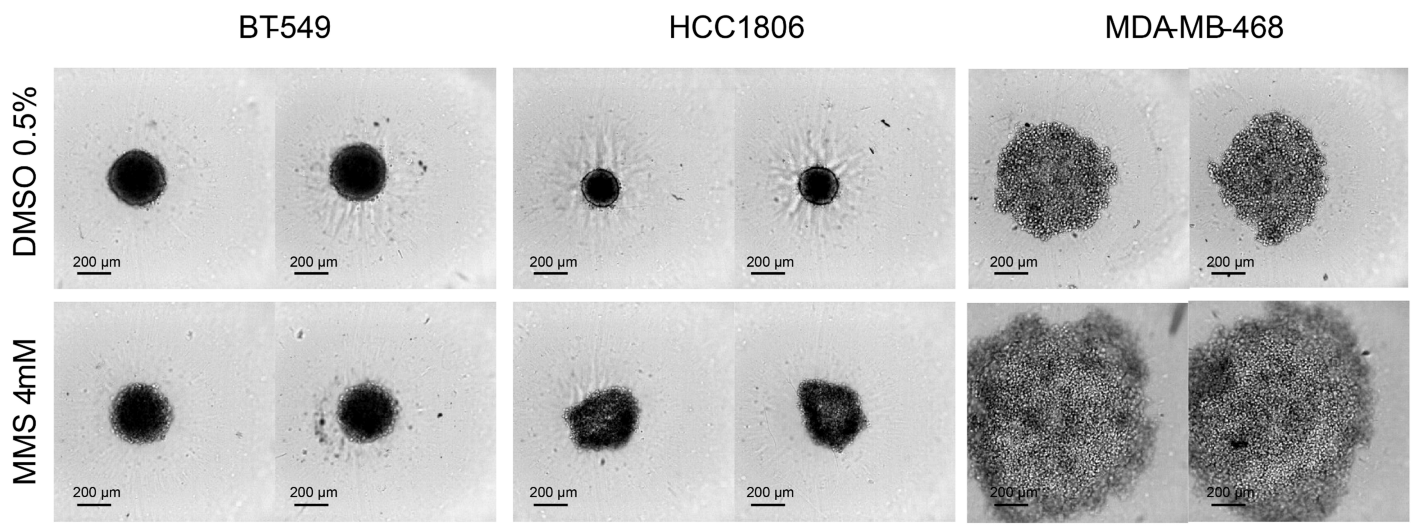

Figure 1

Brightfield HCI of BT-549, HCC1806, and MDA-MB-468 spheroids cultured in 384-well plates treated for 72 h with vehicle (DMSO 0.5%) or positive control (4 mM MMS). Images acquired at 10x magnification with the Operetta CLS™ High Content Analysis system (Revvity). Scale bars: 200 µm.

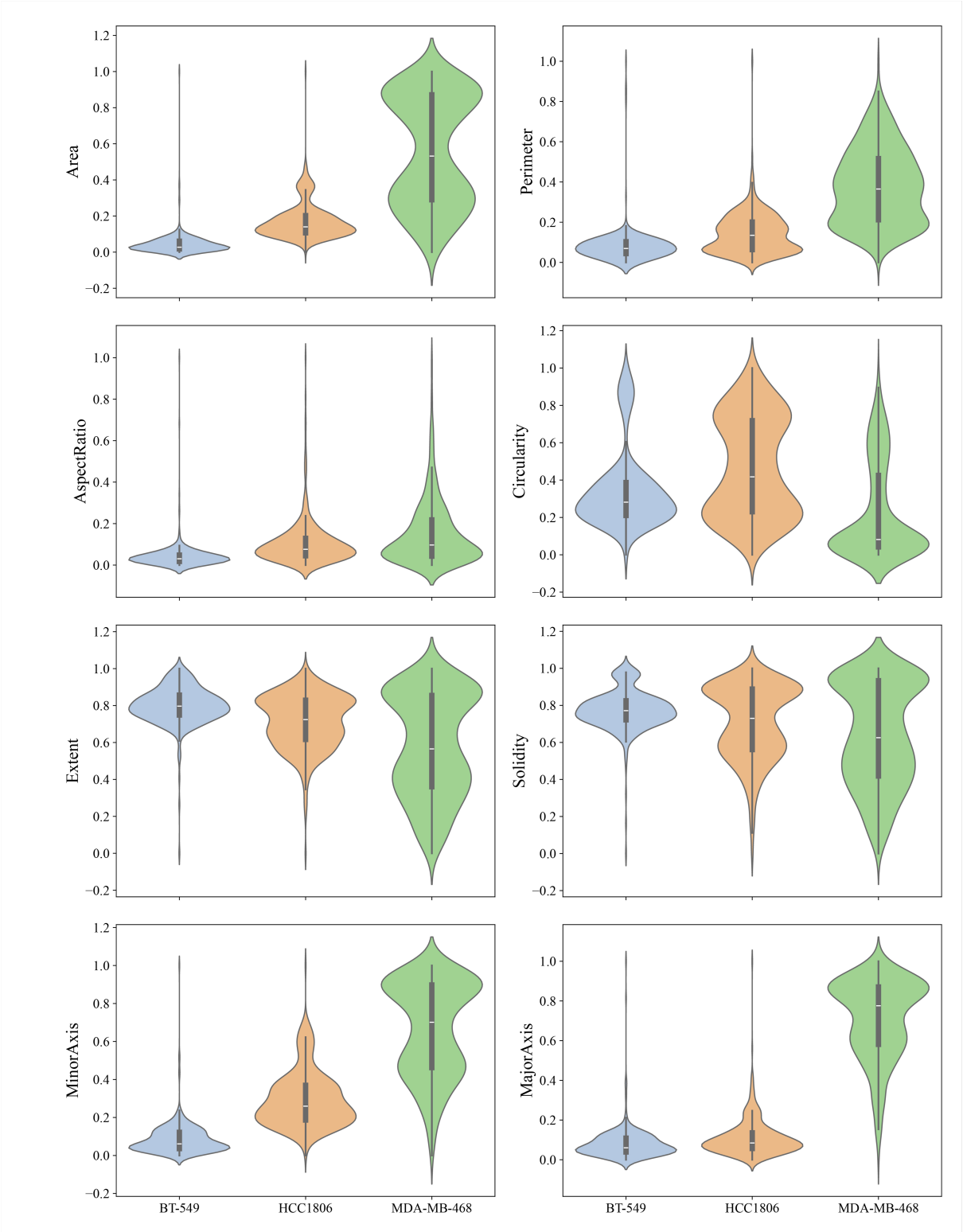

Figure 2

Violin plots of representative normalized morphological features extracted at 72 h post-treatment for BT-549 (blue), HCC1806 (orange), and MDA-MB-468 (green) spheroids. Violin plots illustrate distinct spheroid architectures across cell lines. Displayed features include projected area, perimeter, circularity, solidity, extent, aspect ratio, and major and minor axes. Figures were generated in Python 3.10 using *matplotlib* and *seaborn*. [8,9] In-plane morphological features are computed in pixel units (px for lengths;

px² for areas); while circularity, solidity, extent, and aspect ratio are dimensionless. Feature values were normalized to the [0,1] range using the *MinMaxScaler* function from *scikit-learn* (v1.2.2)



Figure 3

Histogram of normalized distributions of representative features across BT-549, HCC1806, and MDA-MB-468 spheroid replicates at 72 h post-treatment. Data were extracted from three independent

replicate plates (R1, R2, R3) using a consistent segmentation and feature extraction pipeline. Within each plate, 48 intra-plate technical replicates were included per condition. *MinMax* normalization was applied within each replicate prior to visualization. The overlapping distributions demonstrate reproducible feature measurements across replicates, while minor deviations are consistent with expected biological or technical variation.

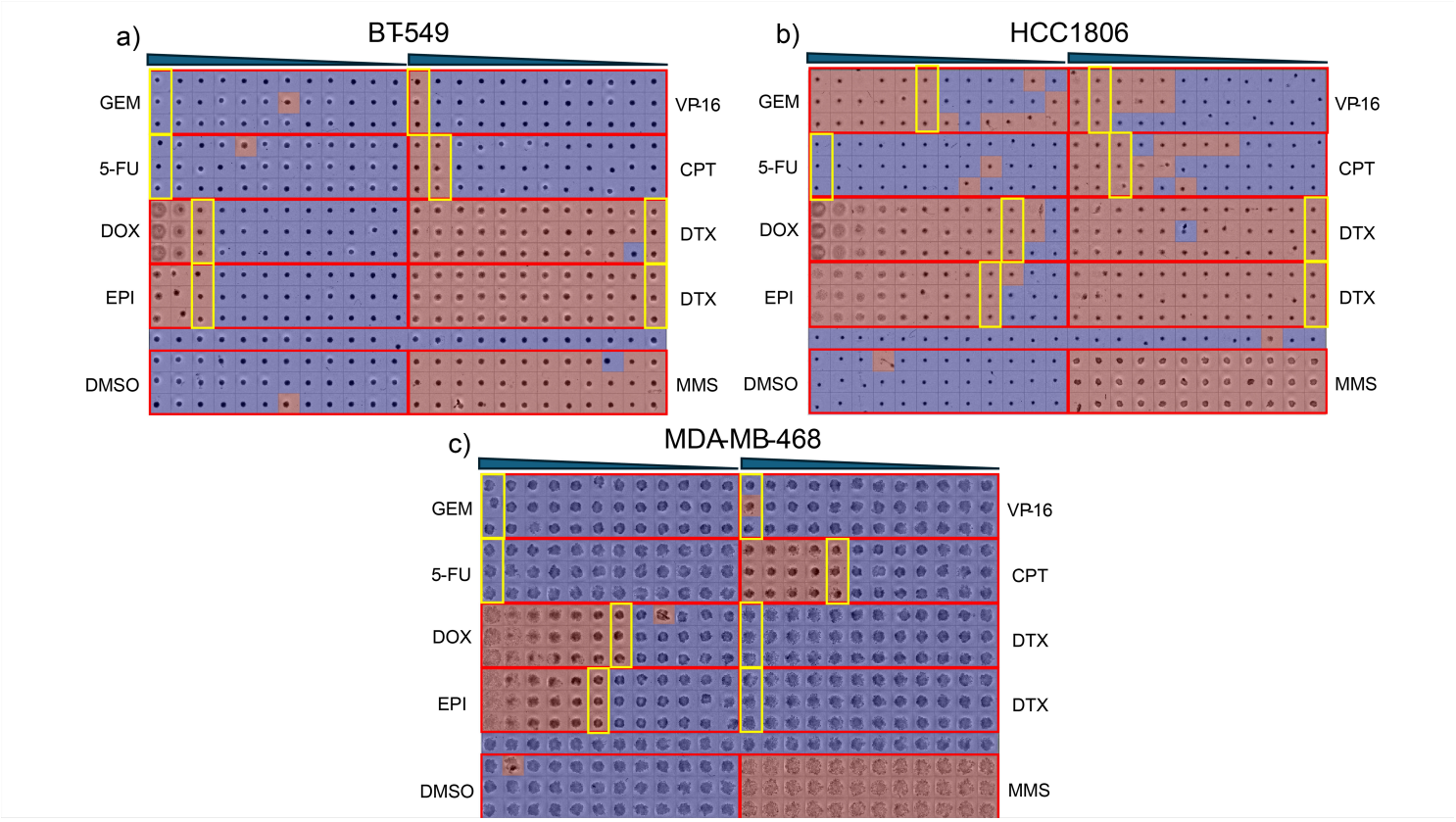

Figure 4

Color-coded representation of drug-induced effect to determine MDC in assay plates with 3D spheroids. Heatmaps showing the clustering-based classification of morphological disruption across 12-point dose–response experiments for the eight chemotherapeutic agents in BT-549 (a), HCC1806 (b), and MDA-MB-468 (c) spheroids. Individual wells of the 384-well plate are colored according to UMAP+k-means (k=2) cluster assignment: red indicates a disrupted (affected) spheroid morphology, and blue indicates intact (non-affected) spheroids. Yellow boxes outline the MDC (minimal dose to clusterize as affected). Rows correspond to each compound tested; columns represent increasing dilution points. A total of 12 concentrations were used for each drug. Note that starting concentrations were different for each drug: GEM 100 µM, 5-FU 200 µM, DOX 250 µM, EPI 110 µM, VP-16 50 µM, CPT 10 µM, DTX 1 µM, PTX 10 µM. Subsequent 1:2 serial dilutions were performed. Each dose was assayed in triplicate in each plates and three independent plates were assayed for each cell line. Every plate included 48 control wells treated with vehicle DMSO 0.5% and 48 wells treated with MMS 4 mM.

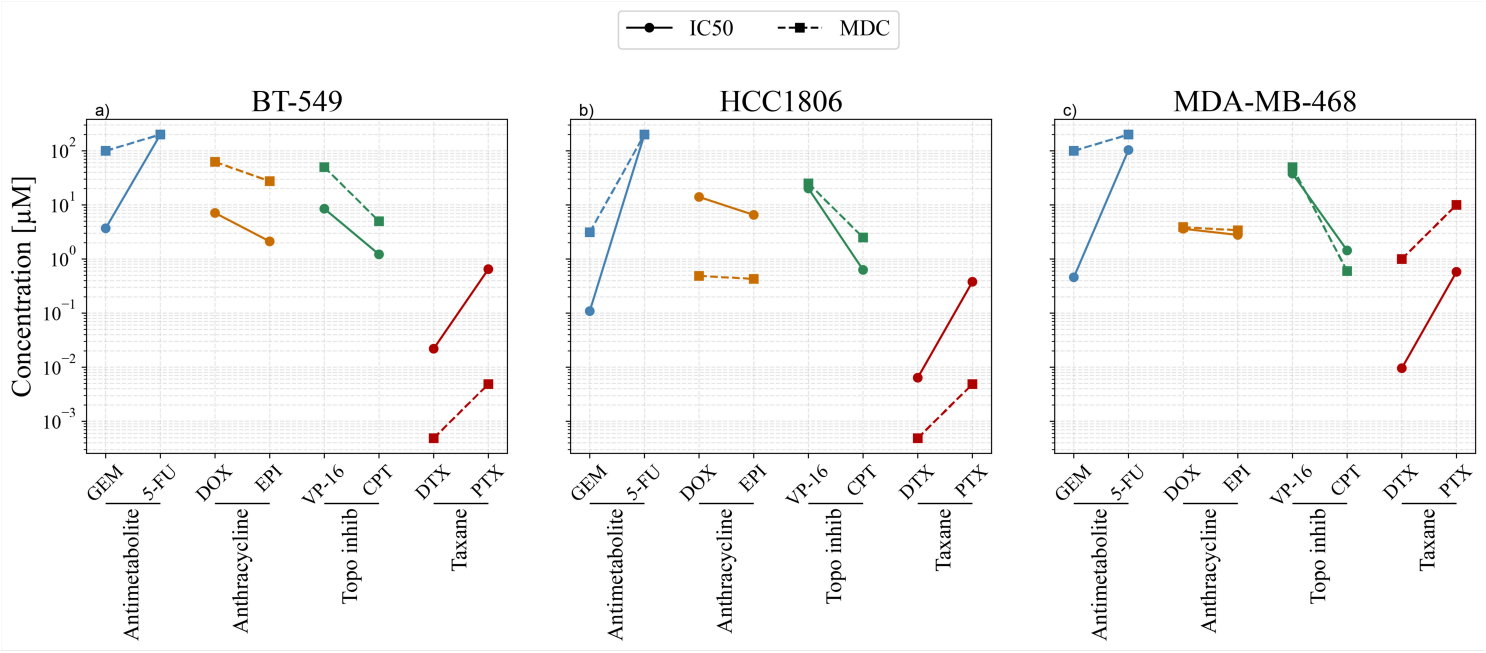

Figure 5

Comparison of EC_{50} and MDC concentrations for eight chemotherapeutic agents across the three TNBC cell lines a) BT-549, b) HCC1806, and c) MDA-MB-468. Compounds are grouped by pharmacological class according to their MoA: antimetabolites (blue), anthracyclines (yellow), topoisomerase inhibitors (green), and taxanes (red). The potency of each drug class in 2D and 3D is represented by the EC_{50} values (circles, solid lines) and MDC values (squares, dashed lines) respectively.

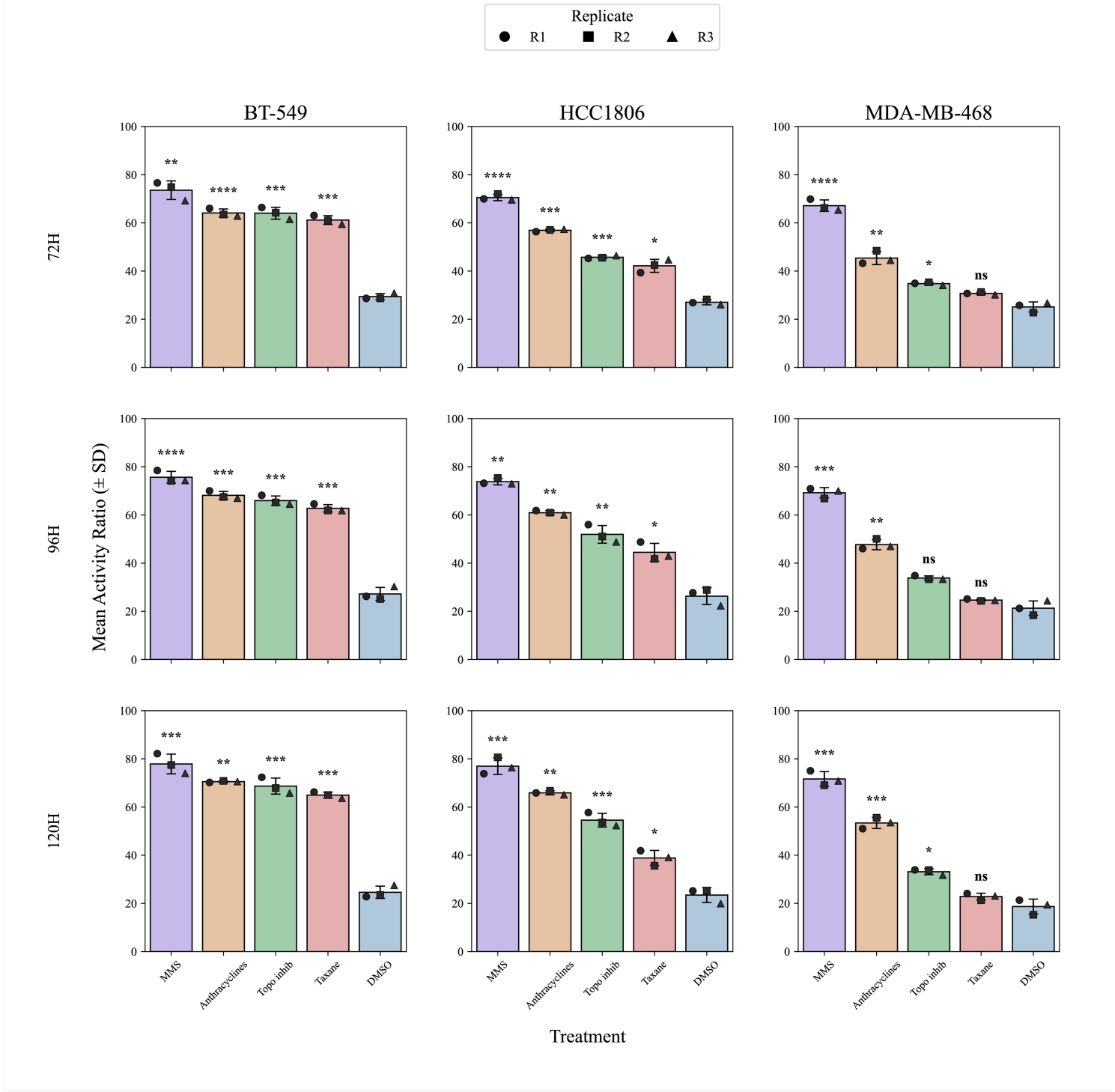

Figure 6

Phenotypic changes across TNBC spheroids treated with drugs over time. Bar plots show the AR (mean ± SD) for each treatment condition in BT-549, HCC1806, and MDA-MB-468 spheroids, measured at 72 h, 96 h, and 120 h post-treatment. Each bar reflects the average AR per treatment across intra-plate replicates, three overlaid markers indicating each replicate (R) plate: R1 (black circle), R2 (black square), and R3 (black triangle). Error bars correspond to SD among plates. The AR quantifies the relative displacement of the phenotypic centroid of each spheroid compared to the DMSO (intact) and MMS

(disruptive) phenotypic centroids (0≈DMSO, 100≈MMS). Statistical comparisons were performed *versus* DMSO using Welch's t-test with Bonferroni correction; significance levels are annotated as **** $p < 0.0001$, *** $p < 0.001$, ** $p < 0.01$, * $p < 0.05$, ns (not significant).

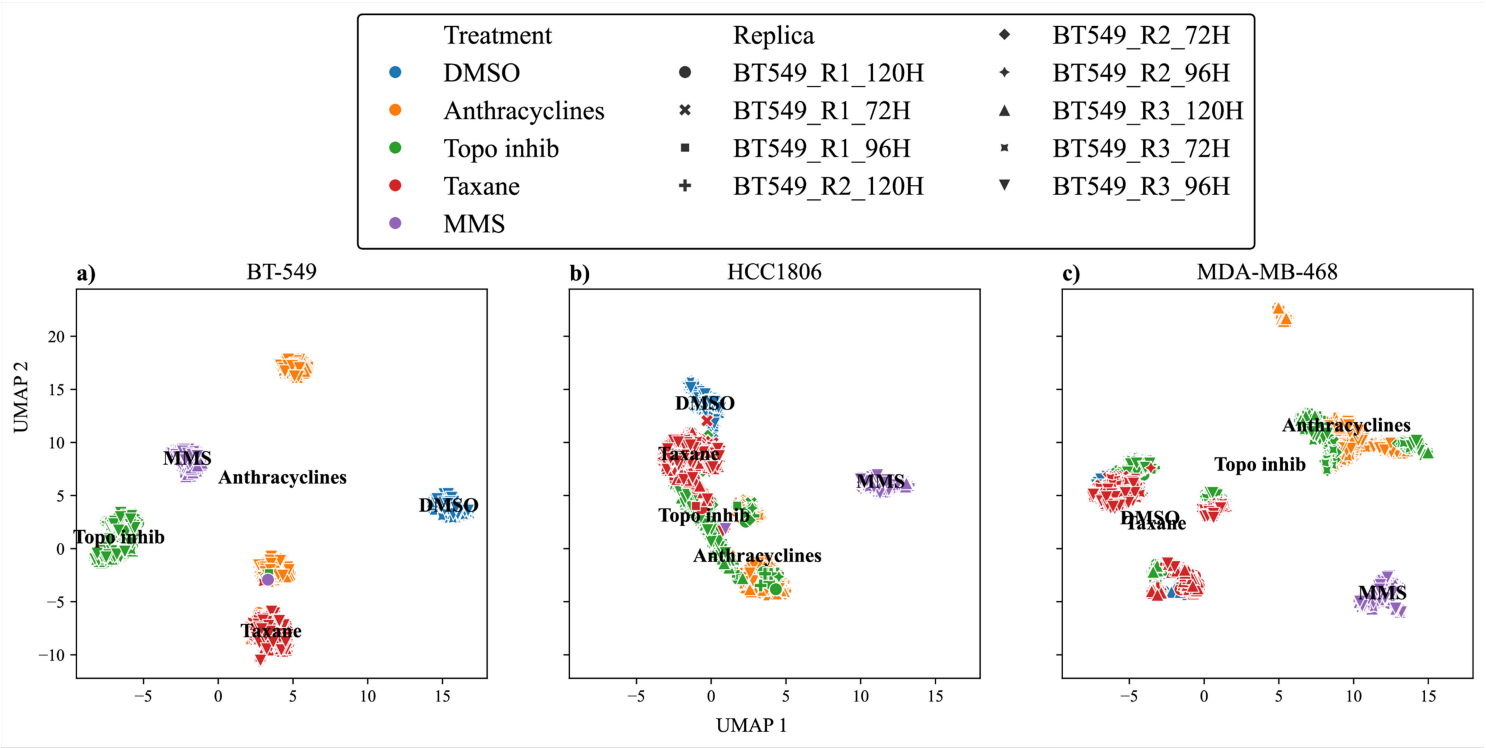

Figure 7

Combined UMAP projections of spheroid morphometric features across all plates, replicates, and timepoints for each cell line: a) BT-549, b) HCC1806, c) MDA-MB-468. Each marker symbol denotes a distinct replicate–timepoint combination, while colors represent treatment groups (DMSO = blue, anthracyclines = orange, topoisomerase inhibitors = green, taxanes = red, and MMS = purple). Feature data were standardized by z-score normalization after removing three-standard-deviation outliers per treatment. UMAP was configured with n_neighbors=15 and min_dist=0.1 to preserve local and global structures. No additional clustering was applied: the treatment-driven grouping is directly visualized in the UMAP embedding.

Supplementary Files

This is a list of supplementary files associated with this preprint. Click to download.

- SupplementaryFigure1.png
- SupplementaryFigure2.png
- SupplementaryFigure3.png